Effects of externally applied stress on multiphase flow characteristics in naturally fractured tight reservoirs.

HAWEZ, H.K. and ASIM, T.

2024

applied sciences

MDPI

Article

Effects of Externally Applied Stress on Multiphase Flow Characteristics in Naturally Fractured Tight Reservoirs

Haval Kukha Hawez [1,2] and Taimoor Asim [2,*]

[1] Department of Petroleum Engineering, Faculty of Engineering, Koya University, Koya KOY45, Kurdistan Region—F.R., Iraq; haval.hawez@koyauniversity.org
[2] School of Computing, Engineering, and Technology, Robert Gordon University, Aberdeen AB10 7GJ, UK
* Correspondence: t.asim@rgu.ac.uk

Abstract: Externally applied stress on the rock matrix plays a crucial role in oil recovery from naturally fractured tight reservoirs, as local variations in pore pressure and in-situ tension are expected. The published literature severely lacks in evaluations of the characteristics of hydrocarbons, displaced by water, in fractured reservoirs under the action of externally applied stress. This study intends to overcome this knowledge gap by resolving complex time- and stress-dependent multiphase flow by employing a coupled Finite Element Method (FEM) and Computational Fluid Dynamics (CFD) solver. Extensive three-dimensional numerical investigations have been carried out to estimate the effects of externally applied stress on the multiphase flow characteristics at the fracture–matrix interface by adding a viscous loss term to the momentum conservation equations. The well-validated numerical predictions show that as the stress loading increases, the porosity and permeability of the rock matrix and capillary pressure at the fracture–matrix interface decrease. Specifically, matrix porosity decreases by 0.13% and permeability reduces by 1.3% as stress increases 1.5-fold. Additionally, stress loading causes a decrease in fracture permeability by up to 29%. The fracture–matrix interface becomes more water-soaked as the stress loading on the rock matrix increases, and thus, the relative permeability curves shift to the right.

Keywords: multiphase flow; structural mechanics; rock mechanics; naturally fractured tight reservoir; finite element method; computational fluid dynamics; fracture-matrix interface

Citation: Hawez, H.K.; Asim, T. Effects of Externally Applied Stress on Multiphase Flow Characteristics in Naturally Fractured Tight Reservoirs. *Appl. Sci.* **2024**, *14*, 8540. https://doi.org/10.3390/app14188540

Academic Editor: Zhaosheng Yu

Received: 23 August 2024
Revised: 11 September 2024
Accepted: 18 September 2024
Published: 23 September 2024

1. Introduction

The exploitation of hydrocarbon resources from subsurface reservoirs has been a cornerstone of modern industrial civilization. As global energy demands continue to rise, the development and optimization of unconventional resources have taken on an increasingly critical role in meeting these demands. Among these unconventional resources, naturally, fractured tight reservoirs have gained significant attention due to their vast hydrocarbon potential. These reservoirs, characterized by low permeability and complex fracture networks, present unique challenges and opportunities for exploration and production. Therefore, the significance of tight reservoirs in the energy industry cannot be overstated. These reservoirs, which encompass a wide range of geological formations, including shale, sandstone, and carbonate rocks, hold vast quantities of hydrocarbons. The exploitation of these resources has transformed the energy landscape, particularly in regions such as North America, where the shale revolution has led to a surge in oil and gas production [1]. One key aspect that has garnered attention in recent years is the effect of externally applied stress on the multiphase flow characteristics within the naturally fractured tight reservoirs.

Tight reservoirs, commonly referred to as unconventional reservoirs, have become the focal point of the energy industry's quest to meet the world's ever-growing energy demands [2]. These reservoirs are characterized by low permeability, which hinders the flow of hydrocarbons through the rock matrix [3]. Consequently, unconventional reservoirs

require advanced drilling and stimulation techniques to make hydrocarbon extraction economically viable [4]. Naturally fractured tight reservoirs, in particular, are a subset of these unconventional reservoirs and possess dual challenges, i.e., their inherent low permeability and the presence of fractures that significantly affect fluid flow [5–7]. The flow of fluids in naturally fractured tight reservoirs is a multifaceted phenomenon, often involving the coexistence of different phases, including oil, gas, and water [8,9]. Multiphase flow in such reservoirs is inherently complex, with interactions between the phases and rock matrix playing a decisive role in determining production performance [10]. The presence of fractures, which serve as preferential pathways for fluid flow, further complicates the picture. While the influence of fractures on multiphase flow in tight reservoirs is well documented, the impact of externally applied stressors has received comparatively less attention. External stresses, including tectonic forces, reservoir compaction, and hydraulic fracturing operations, can alter the subsurface stress field [11,12].

2. Literature Review

Externally applied stress refers to the forces acting on the reservoir rock due to various factors, including tectonic stresses, overburden pressure, and fluid injection or withdrawal [13–15]. External stressors induce reservoir deformation, leading to changes in the rock's mechanical properties, such as porosity, permeability, and fracture aperture [16,17]. These changes, including stress-dependent permeability, porosity, and fracture aperture alterations, have significant implications for reservoir management and ultimately influence the flow of fluids within the reservoir [18–20]. The relationship between externally applied stress and multiphase flow characteristics in naturally fractured tight reservoirs is a complex and multifaceted topic that requires careful investigation because the behavior of multiphase fluids within naturally fractured tight reservoirs is profoundly affected by externally applied stress [21–23]. The interaction between hydrocarbons, water, and rock under stress conditions leads to complex phenomena, including capillary pressure variations, relative permeability alterations, and changes in wettability [24–26]. These factors have a direct impact on reservoir production rates and ultimate recovery. Understanding how these external stresses affect fluid flow through fractures is crucial for optimizing production and reservoir management.

Understanding how externally applied stress influences multiphase flow within naturally fractured tight reservoirs is essential for several reasons. First, it can provide valuable insights into reservoir behavior, which can inform reservoir management strategies and enhance hydrocarbon recovery [27,28]. Second, it can help mitigate the risks associated with hydraulic fracturing operations, ensuring that fractures propagate in a controlled manner and do not interfere with nearby wells or environmental factors [29,30]. Third, it can contribute to the development of advanced modelling and simulation tools that can predict reservoir response to stress changes, leading to more accurate reservoir performance predictions [31].

There are numerous numerical approaches for modelling poroelastic issues. Gao et al. [32], for example, developed a coupled stress and reservoir simulator with a staggered grid Finite Difference Method (FDM) to improve wellbore stability. On the other hand, Sangnimnuan et al. [33] developed a coupled fluid–flow/stress model to forecast stress evolution using the Finite Volume Method (FVM) in unconventional reservoirs. Ashworth and Doster [34] have reported a similar implementation of FVM because of the advantage of full cell-centered variables across fluid flow and solid mechanics. Furthermore, due to its robustness in solving diverse solid mechanics equations, the Finite Element Method (FEM) is a popular alternative, and it has been widely employed in the literature to tackle complex poroelastic situations [35]. Many research efforts and signs of progress have been made toward understanding and modelling fluid flow in fractured porous media in the past half-century. However, most studies focused on the single-phase flow [36–38] without taking into account multiphase flow and an understanding of the phase flow characteristics and development at the fracture–matrix interaction. The fracture–matrix interface is an

important area to consider because it can significantly impact fluid flow in the reservoir. The properties of the interface, such as the roughness and wettability, can affect how fluids move through the fractures and into the matrix. Additionally, the stress applied to the interface can affect the connectivity between the fractures and the matrix, which can impact the overall flow behavior of the reservoir.

The motivation for studying the effects of externally applied stress on multiphase flow characteristics at the fracture–matrix interface in naturally fractured tight reservoirs stems from the increasing importance of unconventional resources in global energy production. As conventional oil and gas reserves continue to decline, unconventional resources, including tight reservoirs, have become a critical component of the energy mix. However, the exploitation of these resources presents unique challenges, including low permeability and complex fracture networks, which can significantly impact production rates. Recently, due to decreased production rates and unfavorable recovery factors during hydrocarbon production, there has been an increased focus on the characterization of multiphase fluid flow behavior under different stress loadings at the fracture–matrix interface. Further research and advancements in numerical modelling techniques are needed to accurately capture the complex phenomena associated with production from tight reservoirs, including the impact of fractures, stress changes, and multiphase flow interactions. For precise oil recovery predictions, this research aims to establish the connection between external stress and multiphase flow at the fracture–matrix interface in naturally fractured tight reservoirs.

3. Materials and Methods

In this study, a coupled Finite Element Method–Computational Fluid Dynamics (FEM–CFD) model to investigate the effect of externally applied stress on multiphase flow in tight reservoirs is proposed. The numerical model has been developed using ANSYS® 2024 R2 modules for fluid flow (CFD: FLUENT) and solid mechanics (FEA: Static Structural).

3.1. Geometry of Naturally Fractured Tight Reservoir

The core scale (Darcy scale) is chosen to represent fractured tight reservoirs in this study. Figure 1a,b depicts the three-dimensional geometry of the sample tight reservoir. The sample's geometric design is based on Clashach's Core Flood laboratory experiments, which will be used later for validation purposes. The core sample resembles a cylinder, with a rectangular fracture region in the middle. The diameter of the core (D) is 3.79 cm, while its length (L) is 7.54 cm. The aperture (h) of the fracture is 130 μm. Both regions have been modelled such that fluid flow can take place in them.

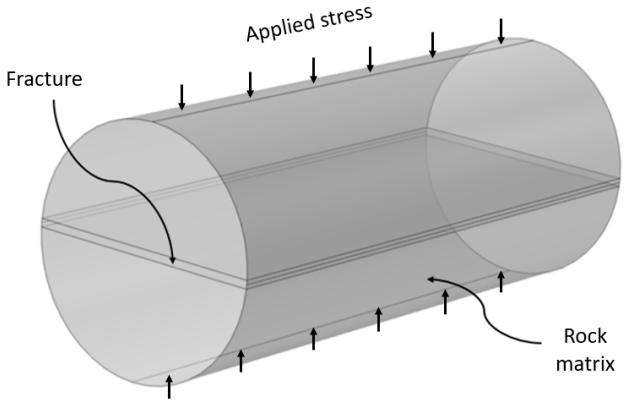

(**a**)

Figure 1. *Cont.*

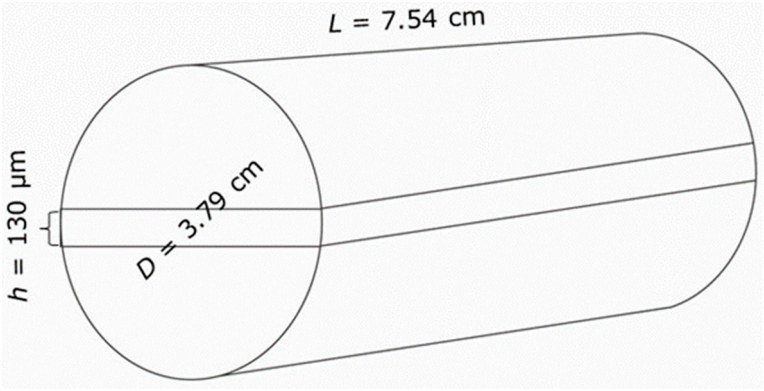

(**b**)

Figure 1. Naturally fractured tight reservoir sample: (**a**) 3D model; (**b**) geometric dimensions.

3.2. Meshing of the Flow Domain

The flow domain has been spatially discretized with an unstructured tetrahedral to reduce the skewness of the mesh elements, as shown in Figure 2a. The mesh density has been kept significantly higher in the aperture region as it is the primary area of interest in the current investigations. In order to ensure that the numerically predicted results are independent of the mesh sizing used [39,40], five different meshes have been generated and compared for accuracy in predicting the multiphase flow behavior at the fracture–matrix interface. These meshes correspond to element sizes of 5 mm, 3.5 mm, 2.8 mm, 2 mm, and 1.8 mm. The resulting number of elements in the flow domain is summarized in Table 1.

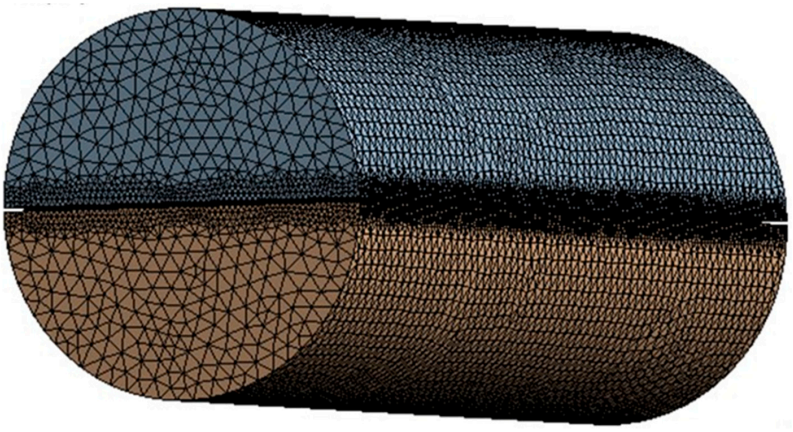

(**a**)

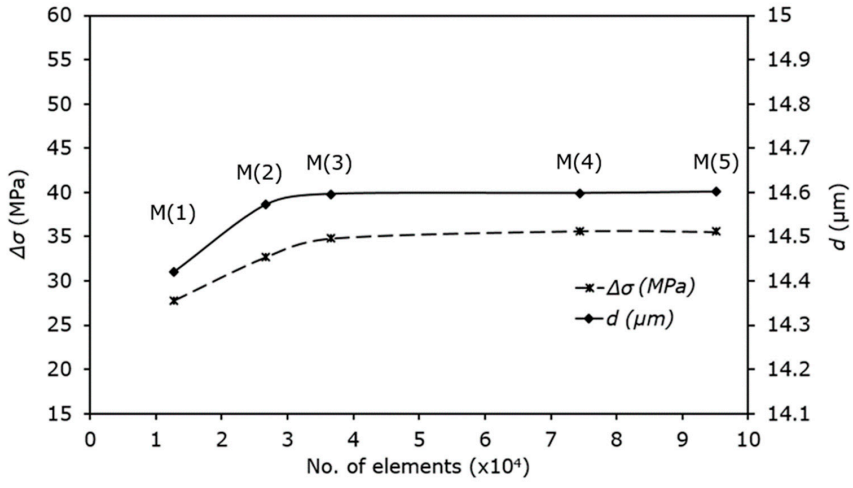

(**b**)

Figure 2. The meshing of the flow domain: (**a**) mesh M(3); (**b**) mesh sensitivity analysis results.

Table 1. Meshes generated in the flow domain.

Mesh	Total Number of Elements
M(1)	1.27×10^4
M(2)	2.7×10^4
M(3)	3.7×10^4
M(4)	7.4×10^4
M(5)	9.5×10^4

The mesh sensitivity analysis results are shown in Figure 2b. It can be seen that as the number of mesh elements increases from M1 to M3, the stress fluctuations ($\Delta\sigma$) and overall displacement of the rock matrix (d) increase. When the number of mesh elements increases from M3 to M5, there is a negligibly small change in $\Delta\sigma$ and d. Thus, it is clear from the mesh sensitivity analysis that M3 (shown in Figure 2a) is the most suitable mesh and accurately predicts the petrophysical properties of naturally fractured tight reservoirs, and hence it has been chosen to conduct further investigations in this study.

3.3. Multiphase Flow Modelling in Naturally Fractured Tight Reservoir

The multiphase flow within the naturally fractured tight reservoir sample has been modelled using the Volume of Fluid (VOF) method. The VOF model is a free-surface modelling technique that can locate and monitor fluid–fluid interfaces, with the present one occurring between oil and water. The saturation (S) of each fluid phase is determined in the control volumes; the sum of S for all fluid phases present is equal to 1. When a control volume is filled with oil, the saturation of oil is 1 (i.e., $S_o = 1$), while the saturation of water is 0 (i.e., $S_w = 0$). Thus, if a control volume contains a mixture of both oil and water, S_o and S_w are between 0 and 1, and $S_m \neq 0$.

Both the rock matrix and the fracture zone have been modelled as porous media. In the real world, a porous material consists of many tortuous routes (or pores) with varying flow velocity vectors. When a porous media is numerically modelled, as in this study, no such routes exist. This is introduced indirectly in the modelling by defining the porosity (φ) and permeability (k) of the material. The resulting mass conservation equation can thus be written as [41]:

$$\frac{\partial}{\partial_t}(\varphi\, S_\beta\, \rho_\beta) + \nabla\cdot\left(\varphi\, S_\beta\, \rho_\beta\, \vec{U_\beta}\right) + \frac{\mu}{k}\, \vec{U_\beta} = 0 \tag{1}$$

where β represents the phase. The third term in the equation is the source term representing viscous losses due to Darcy effects. The same viscous loss term is added to the momentum conservation equation as well.

The momentum conservation equation is given as:

$$\left(\frac{\varphi}{k_f} + (\alpha_B - \varphi)\frac{1-\varphi}{K_d}\right)\frac{\partial(S_\beta \rho_\beta p_\beta)}{\partial t} - \nabla\cdot\left(-\frac{k_a Kr_\beta\, \rho_\beta}{\mu_\beta}(\nabla P_\beta - \rho_\beta g \nabla D)\right) = \rho_\beta \alpha_B\left(\frac{\partial \varepsilon_{vol}}{\partial t}\right) \tag{2}$$

The mixture density (ρ_m) and the mixture dynamic viscosity (μ_m) are given as [41]:

$$\rho_m = S_w\, \rho_w + (1 - S_w)\, \rho_o \tag{3}$$

$$\mu_m = S_w\, \mu_w + (1 - S_w)\, \mu_o \tag{4}$$

3.4. Modelling of Applied External Stress in Naturally Fractured Tight Reservoir

Externally applied stress loading has a significant impact on the multiphase flow and thus on oil recovery from naturally fractured tight reservoirs. When the rock is subjected to compressive stresses, although it stays reasonably stiff with low volumetric deformation, the vacant spaces (such as fractures) undergo geometric strain. The strain is sufficiently small because the rock behaves like a linear elastic material [42,43]. The rock deformation can be described using the stress–strain relationship, i.e., Hooke's law, as [44]:

$$\Delta\sigma^{el} = C\,\Delta\varepsilon^{el} \tag{5}$$

where σ^{el} is the elastic stress tensor, ε^{el} is the elastic strain tensor, and C is the linearized elastic stiffness tensor, provided by the bulk (K_b) and shear (R) modulus as [45]:

$$C = K_b\,I + 2\,R\,I_{dev} \tag{6}$$

where I is the second-order identity tensor and I_{dev} is the 4th-order deviatoric projection tensor. Furthermore, changes in pore spaces are proportional to the logarithmic pressure [46] when the rock is subjected to elastic stress loading, which can be expressed as:

$$\Delta e^{el} = -X\,\Delta\left(ln\left(\sigma + \zeta_t^{el}\right)\right) \tag{7}$$

where e^{el} is the elastic pore space (or void ratio), X is the swell index of rock material, σ is the mean effective stress (MPa), and ζ_t^{el} is the elastic limit of the tensile strength.

Void spaces cause non-linear behavior in the porous medium, resulting in changes in the void ratio; therefore, the void spaces' dimensions change during stress loading [47,48]. Hence, a non-linear elastic model called the porous elastic model is employed in the present study [49]. The relationship between the elastic void ratio (e^{el}) and the elastic volumetric strain (ε_{vol}^{el}) is given as [50,51]:

$$\varepsilon_{vol}^{el} = ln\left(\frac{1+e^{el}}{1+e_i}\right) \tag{8}$$

where e_i is the initial void ratio. Substituting the porous elasticity relationship (7) into (8) provides the mean effective stress (σ) as a function of the elastic volumetric strain, as:

$$\sigma = -\zeta_t^{el} + \left(\sigma_i + \zeta_t^{el}\right)\,exp\left(\frac{1+e_i}{X}\left(1 - exp\left(\varepsilon_{vol}^{el}\right)\right)\right) \tag{9}$$

where σ_i is the initial mean stress.

The bulk modulus (K_b) is also based on the stress and elastic volumetric strain [52] and can be expressed as:

$$K_b = \left(\sigma + \zeta_t^{el}\right)\left(\frac{1+e_i}{X}exp\left(\varepsilon_{vol}^{el}\right)\right) \tag{10}$$

The shear modulus (R) also depends on the void ratio and pressure indirectly because Poisson's ratio (ν) is a constant [53,54]. The shear modulus can be expressed as:

$$R = \frac{3\,k_b\,(1-2\nu)}{2(1+\nu)} \tag{11}$$

3.5. Material Properties

The two fluids being considered are oil and water, as in the case of Clashach's Core Flood experiments [55]. They have densities of ρ_o = 846 kg/m^3 and ρ_w = 1000 kg/m^3, respectively. The dynamic viscosities of oil and water ($_o$ and $_w$) are 0.00046 Pa·s and 0.001 Pa·s, respectively. The rock matrix has been considered as a porous medium in the present study, having a porosity (φ) of 15.4%, permeability (k) of 315 mD and density of 2500 kg/m^3. Furthermore, the pore size distribution index (λ_p) in the core region is taken as 0.674, and the entry capillary pressure (Pc) is 345 Pa. The fracture region is also modelled as a porous medium with a porosity and permeability of 100% and 3.1 × 10^5 mD, respectively. The Poisson's ratio specified in the present study is 0.14, and the Young's Modulus is 40 GPa. The swell index is 0.0052 [56].

3.6. Initial and Boundary Conditions

The initial and boundary conditions specified in the numerical solver are based on Clashach's Core Flood laboratory experiments [55]. The solver is initialized with S_o = 1

within the flow domain. This means that both the core and fracture regions are filled with oil before starting the solution. The fracture inlet has been modelled as a velocity inlet, with a water injection velocity (U) of 3.9×10^{-5} m/s, resulting in Re~3, and thus Laminar flow modelling has been employed. The outlet of the fracture region has been modelled as a pressure outlet, with atmospheric pressure conditions specified [57,58]. The rest of the flow boundaries have been modelled as stationary walls. External stress loading of 21.4 MPa (from Clashach's experiments), 6.9 MPa, 9 MPa, 11 MPa, 13.1 MPa, 15.2 MPa, and 17.2 MPa have been considered for numerical investigations in the present study.

4. Numerical Solution Strategy

The time-dependent solution strategy adopted in the present study is based on the volume of water being injected from the inlet. Based on the fracture's geometric dimensions and the water injection velocity, the volumetric flow rate is computed. From this, the total volume of water being injected (V_w) in the flow domain for specific time intervals is calculated. The time step size used in the present study is 0.1 s, while the solution data are saved when the injected volume of water is equal to 10% of the pore volume (i.e., 10% of the volume of all the pores together). This is then repeated for 20%, 30%, 40%, 50%, 60%, and 70% of the pore volume.

The FEM–CFD coupling strategy adopted in the present study is shown in Figure 3. The coupled FEM–CFD model enables the evaluation of the dependence of multiphase flow parameters on externally applied stress in naturally fractured tight reservoirs. It can be seen that the FEM-predicted geomechanical parameters (displacement and strain) are used to calculate the updated porosity, permeability, and fracture aperture. These are then input in the CFD model, which is solved iteratively w.r.t. time in order to obtain flow parameters of interest, such as the saturation of both phases. CFD-predicted flow parameters are then used to calculate the capillary pressure and relative permeability using Brook's and Corey's method.

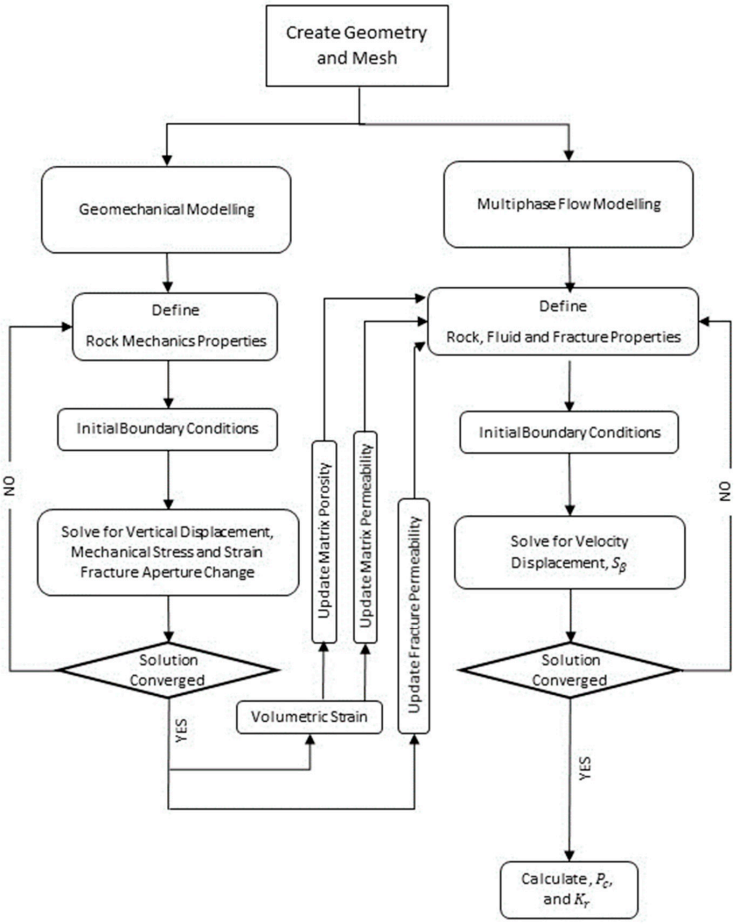

Figure 3. Coupled FEM–CFD solution strategy.

Numerical Model Validation

The coupled FEM–CFD numerical model developed in the present study has been validated against Clashach's Core flooding experimental data. The experimental data on the cumulative outflow of oil (Qc) are based on differential pressure (ΔP) applied throughout the sample reservoir, while the core sample is subjected to an external stress of 21.4 MPa. Figure 4 depicts the results of the numerical model validation where it can be seen that both the numerically predicted and experimental Qc increase with increasing ΔP, and the two agree well with an average difference of <9%. Thus, it can be concluded that the coupled numerical model developed here captures the stress-dependent multiphase flow characteristics within a sample of the naturally fractured tight reservoir with reasonable accuracy, and hence it has been used for further scientific investigations.

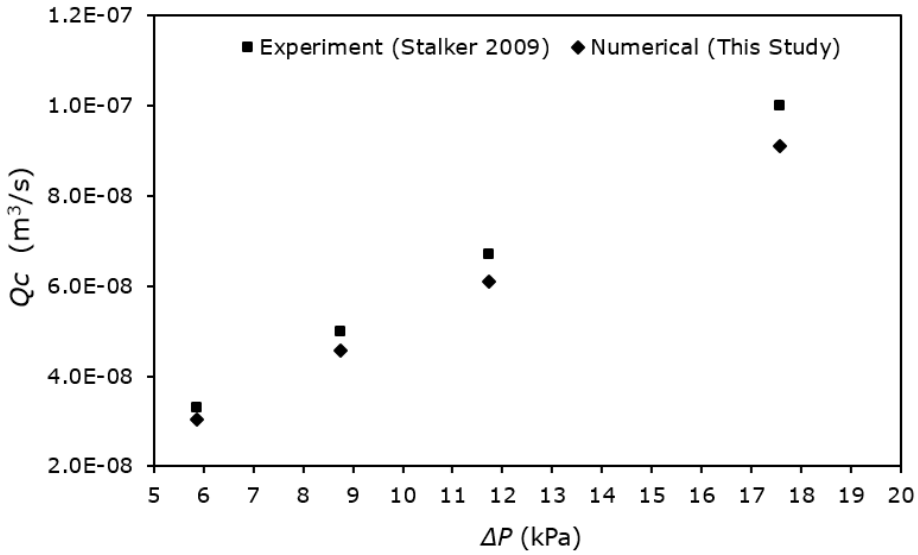

Figure 4. Numerical and experimental cumulative outflow of oil at various differential pressures [55].

5. Results

Based on detailed numerical investigations, the effects of externally applied stress on the geomechanical (porosity and permeability) and multiphase flow (saturation, capillary pressure, and relative permeability) characteristics of naturally fractured tight reservoirs have been analyzed. Special attention has been given to these at the fracture–matrix interface.

5.1. Stress-Dependent Matrix Porosity

Porosity is conventionally obtained through physical testing such as saturation tests [59]. As the core undergoes compaction, its porosity (φ) changes due to the volumetric strain (ε_{vol}), resulting in geometric variations in the pore spaces, while the solid regions remain intact. The porosity of the sample can be obtained through constitutive models, such as [60,61]:

$$\varphi = \frac{e}{1+e_i} = \frac{e_i - (1+e_i)\,\varepsilon_{vol}}{1+[e_i-(1+e_i)\,\varepsilon_{vol}]} \quad (12)$$

The stress-dependent porosity (φ) variations in the naturally fractured tight reservoir sample are shown in Figure 5. It has been observed that as the external stress loading (σ) increases, the matrix porosity decreases almost linearly, which is expected as observed under real-world conditions [43]. At a stress loading of 6.9 MPa, the porosity is 15.38%. When the stress loading is increased to 9 MPa, the porosity decreases to 15.372%. When further increasing the stress loading to 11 MPa, 13.1 MPa, 15.2 MPa, and 17.2 MPa, the porosity of the core sample decreases to 15.368%, 15.365%, 15.362%, and 15.36%, respectively. Thus, by increasing the stress loading on the reservoir sample 1.5-fold, the matrix porosity decreases by 0.13%.

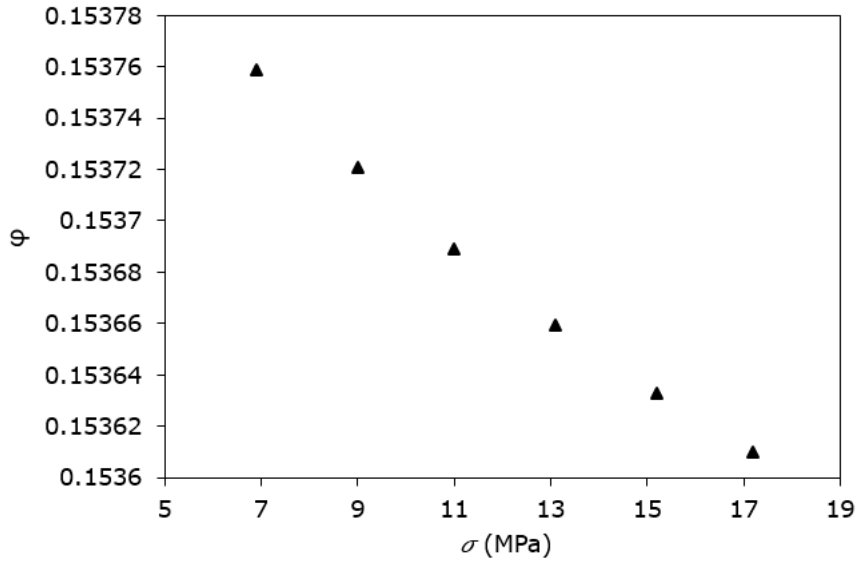

Figure 5. Porosity variations under externally applied stress.

5.2. Stress-Dependent Matrix Permeability

As the rock undergoes compression, the ability of multiphase flow through it changes. The permeability of the rock matrix (k_{mat}) can be expressed as [36]:

$$k_{mat} = k_{i-mat}\left\{1 \pm \frac{1}{2}\left[\frac{9(1-\nu^2)}{2}\left(\frac{\pi\,\Delta\sigma}{E}\right)^2\right]^{1/3}\right\}^2 \tag{13}$$

where k_{i-mat} is the initial rock matrix permeability and E is Young's modulus of the rock matrix. The positive sign refers to dilatational loading, and the negative signal corresponds to the compressional loading [62,63].

Figure 6 depicts the changes in rock matrix permeability under different stress-loading conditions considered in the present study. It can be seen that as stress loading increases, the matrix permeability decreases linearly, a trend which has been observed by Haghi et al. [23] as well as Zhao and Liu [43]. At a stress loading of 6.9 MPa, the matrix permeability is 308.4 mD, which decreases to 307.1 mD as the stress loading increases to 9 MPa. When further increasing the stress loading to 11 MPa, 13 MPa, 15.2 MPa, and 17.2 MPa, the matrix permeability reduces to 306 mD, 305 mD, 304 mD, and 303 mD, respectively.

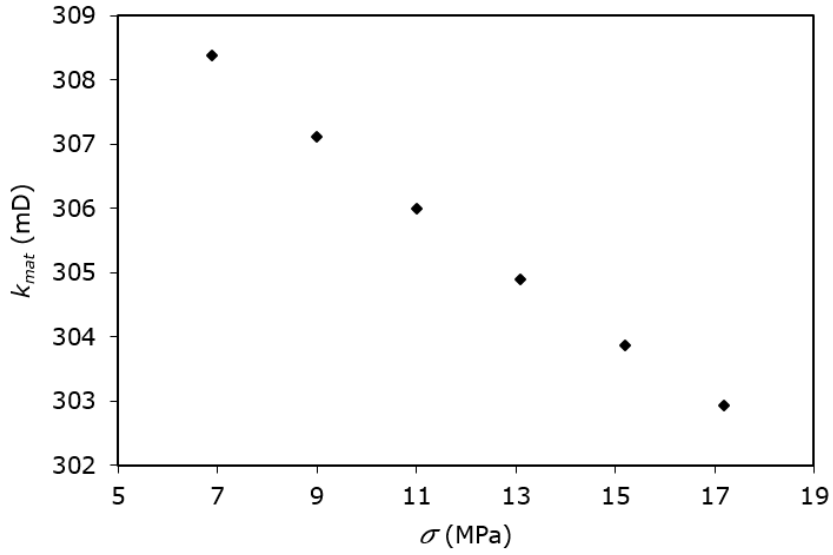

Figure 6. Matrix permeability variations under externally applied stress loading.

Figure 6 indicates that the matrix permeability of 307.1 D in the intact rock reduces to 303 D due to an increase in external stress loading from 6.9 MPa to 17.2 MPa.

5.3. Stress-Dependent Fracture Aperture

As the core sample is subjected to externally applied stress, the fracture aperture is expected to decrease due to the vertical displacement. The fracture aperture's vertical displacement changes spatially along the core radius, i.e., the vertical displacement is less at the core's outer surface and is at a maximum at the core center. These spatial variations in the vertical displacement (δ) along the core radius are depicted in Figure 7a, where $x/X = 0$ represents the outer surface of the core and $x/X = 1$ represents the core's center. As expected, the vertical displacement of the fracture aperture increases when moving inwards toward the core center. It is worth mentioning that the fracture aperture decreases as the external stress increases. The figure clearly shows this behavior, i.e., the rate of increase in vertical displacement is relatively higher along the outer edge of the aperture and gradually decreases towards the core center, where the vertical displacement is at a maximum. This trend has been observed for all the different stress-loading conditions considered. From the un-stressed condition where the (uniform) fracture aperture is 130 µm when an external stress of 6.9 MPa is applied, the average vertical displacement of the fracture region recorded is 21.54 µm, which means that the new mean fracture aperture (h_mean) is 108.46 µm. When increasing the stress loading to 9 MPa, 11 MPa, 13.1 MPa, 15.2 MPa, and 17.2 MPa, the vertical displacement increases to 25.12 µm, 28.05 µm, 30.74 µm, 33.14 µm and 35.19 µm, respectively. Correspondingly, the mean fracture aperture reduces to 104.88 µm, 101.95 µm, 99.26 µm, 96.86 µm, and 94.81 µm, as shown in Figure 7b.

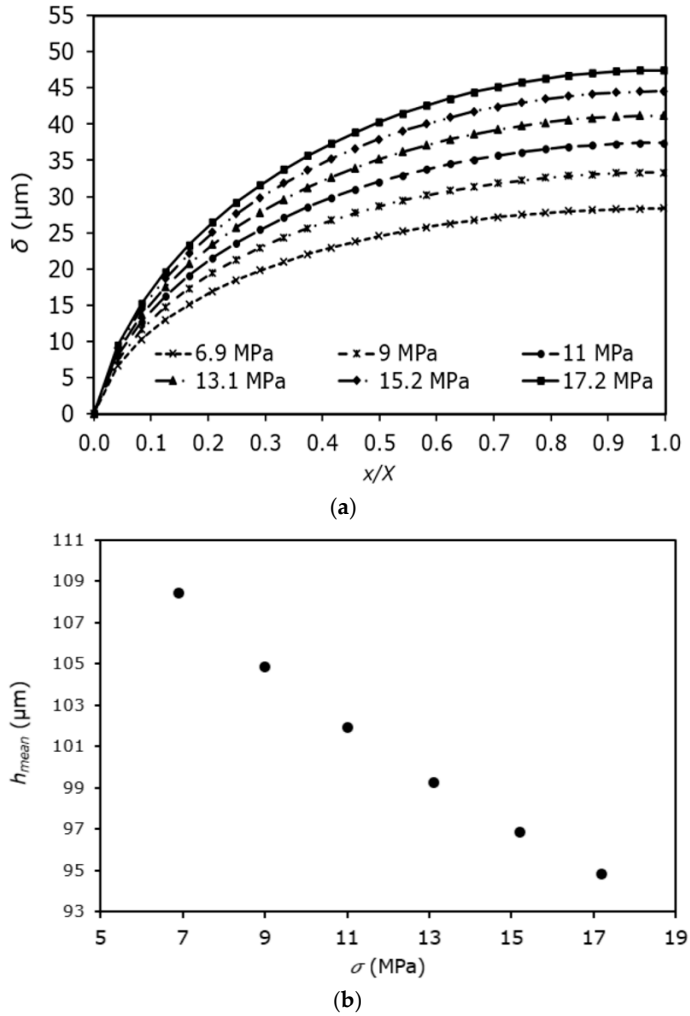

Figure 7. Variations in (**a**) vertical displacement of the fracture aperture along the core radius and (**b**) mean fracture aperture for different stress loadings.

5.4. Stress-Dependent Fracture Permeability

Under stress loading, the permeability of the fracture region also changes [64]. Zhang et al. [65] provide a relationship between the fracture permeability (k_f) and stress-induced fracture aperture change, which can be expressed as:

$$k_f = k_{i-f}\left(1 + \frac{\Delta h}{h_i}\right)^3 \quad (14)$$

where k_{i-f} is the initial fracture permeability and Δh is the change in the fracture aperture after the application of stress, i.e., $\Delta h = h_i - h$.

Figure 8 depicts the variations in fracture permeability (k_f) under different stress-loading conditions. It can be seen that the fracture permeability decreases with increasing stress loading, which is also reported by Cao et al. [17]. The fracture permeability is 180 D at a stress loading of 6.9 MPa. As the stress loading increases to 9 MPa, the fracture permeability reduces to 163 D (9.6% decrease). When further increasing the stress loading to 11 MPa, 15.2 MPa, and 17.2 MPa, the fracture permeability decreases to 150 D (8.1% decrease), 138 D (7.7% decrease), and 128 D (7% decrease). Thus, by increasing the stress loading by 120% (from 6.9 MPa to 17.2 MPa), the fracture permeability decreases by 29%. This provides valuable insights into the relationship between stress loading and fracture permeability, highlighting the importance of considering this relationship when analyzing fractures in tight reservoirs.

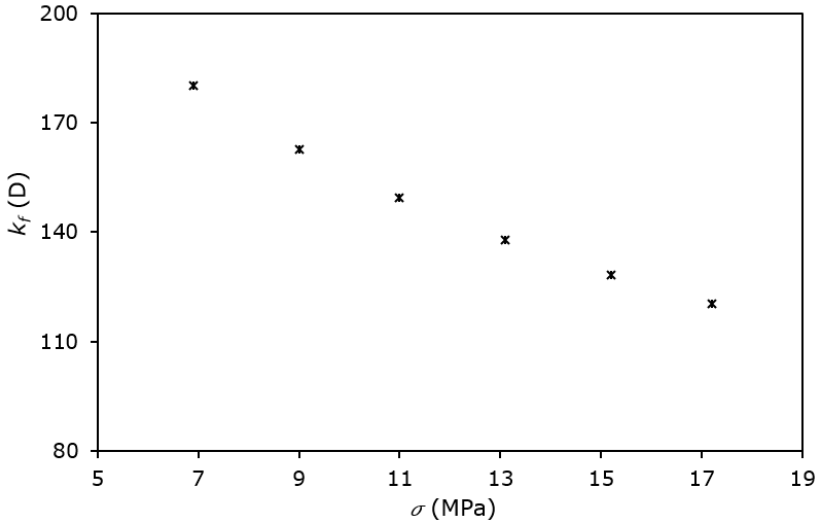

Figure 8. Fracture permeability variations under different stress loadings.

5.5. Stress-Dependent Water and Oil Saturation

Brooks and Corey provide a semi-empirical model for determining the unsaturated hydraulic conductivity [66]. According to this method, the fluid saturation (S) of the phases can be expressed as:

$$S_o = \frac{(S_{oi} - S_{ro})}{(1 - S_{ro} - S_{rw})} \quad (15)$$

$$S_w = \frac{(S_{wi} - S_{rw})}{(1 - S_{ro} - S_{rw})} \quad (16)$$

where the subscripts i and r represent initial and residual, respectively.

Figure 9 depicts the stress-dependent water saturation (S_w) variations at the fracture–matrix interface for various injected water volumes (V_w) under different stress-loading conditions. As the injected water volume increases, water saturation also increases [67,68]. This trend is observed for all different stress-loading conditions considered in this study. S_w = 0.155 at 6.9 MPa stress loading for V_w = 0.1 (or 10%). S_w increases to 0.166, 0.178, 0.191, 0.211, and

0.234 as the stress loading increases to 9 MPa, 11 MPa, 13.1 MPa, 15.2 MPa, and 17.2 MPa, respectively. The same trends have been observed in the case of other water injection values considered here. However, it is worth noting that after V_w = 0.5, the rate of increase in water saturation starts to decrease. This is less prominent at lower stress-loading values and more at higher stress-loading values. The reason for this is evident from the figure, i.e., as V_w increases, S_w increases, approaching S_w = 1, which is the maximum water saturation possible in the rock matrix. As S_w approaches a value of 1, the rate of increase in S_w decreases, and this happens at higher V_w and stress-loading values. Thus, beyond a certain S_w value, further injecting water may not significantly enhance oil recovery.

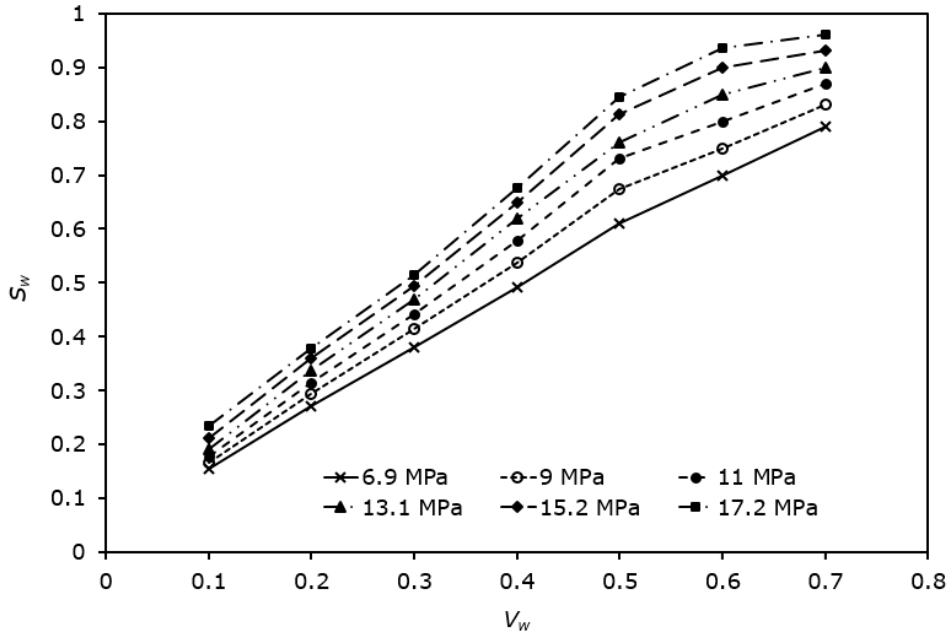

Figure 9. Variations in water saturation at the fracture–matrix interface for different injected water volumes and stress loadings.

5.6. Stress-Dependent Capillary Pressure

The Brooks and Corey method is used to compute the capillary pressure as a function of water saturation at the fracture–matrix interface after running CFD to determine the saturation values. The capillary pressure (*Pc*) can be expressed as:

$$Pc = Pec\ {S_w}^{-1/\lambda_p} \tag{17}$$

where *Pec* is the entry capillary pressure and λ_p is the pore size distribution index.

Figure 10 depicts the variations in capillary pressure concerning the injected water volume (V_w) under different stress-loading conditions. It can be seen that as the volume of injected water increases, the capillary pressure decreases nonlinearly. At lower V_w values, the decrease in the capillary pressure is quite significant due to the highest amount of oil remaining. At higher V_w values, as the capillary pressure approaches close to zero, the stress loading has a negligible effect on it because the capillary forces are dominant. It can be seen that the minimum capillary pressure recorded, at V_w = 0.7, is 0.36 kPa. In terms of stress loading, *Pc* = 5.46 kPa at a stress loading of 6.9 MPa for V_w = 0.1 (10%). *Pc* reduces to 4.96 kPa, 4.47 kPa, 4.01 kPa, 3.47 kPa, and 2.98 kPa at the same V_w when the stress loading increases to 9 MPa, 11 MPa, 13.1 MPa, 15.2 MPa, and 17.2 MPa. The same trend has been observed for other stress-loading conditions considered here.

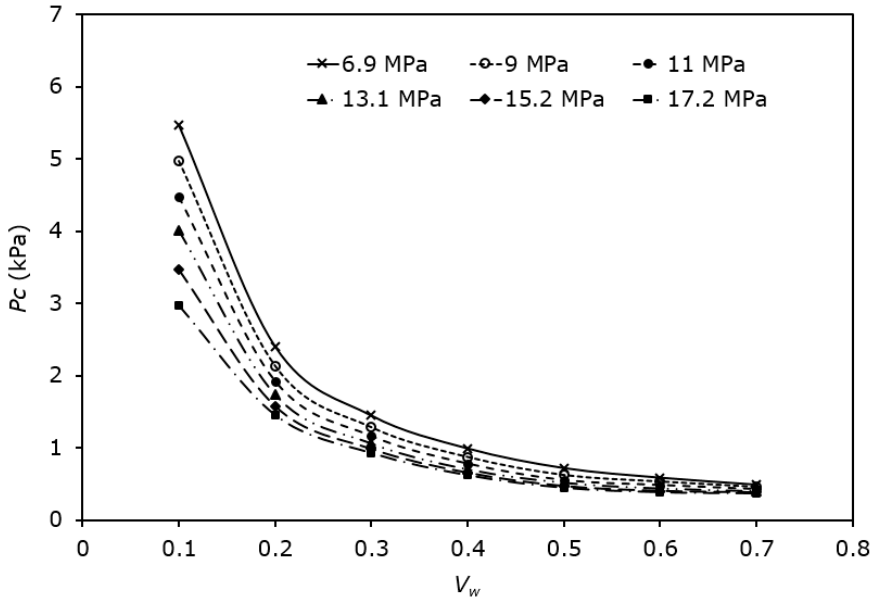

Figure 10. Capillary pressure variations for different injected water volumes and stress-loading conditions.

Further analyzing the effects of external stress on the capillary pressure, Figure 11 depicts capillary pressure variations against stress loading for $V_w = 0.1$. It can be seen that as the stress loading increases, the capillary pressure decreases linearly. Thus, fracture closure with effective stress results in a considerable downward shift in the capillary pressure, leading to an increase in water saturation.

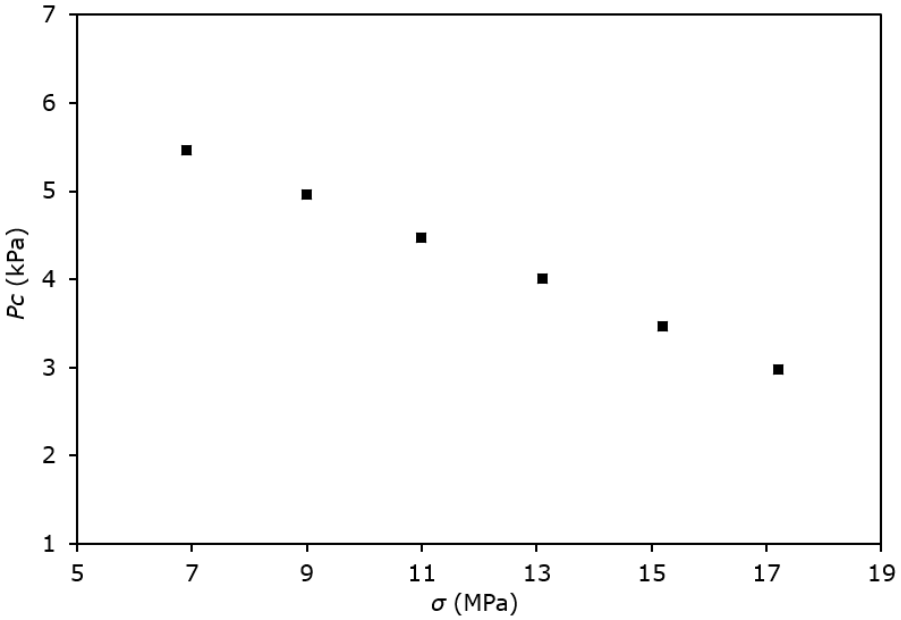

Figure 11. Capillary pressure variations against stress loading at $V_w = 0.1$.

5.7. Stress-Dependent Relative Permeability

The relative permeability is computed as a function of the water saturation and pore size distribution index (λ_p) using the Brooks and Corey method, as below:

$$Kr_w = S_w{}^{(3+2/\lambda_p)} \tag{18}$$

$$Kr_o = (1 - S_w)^2\left(1 - S_w{}^{(1+2/\lambda_p)}\right) \tag{19}$$

The relative permeabilities are computed using the saturation values obtained from the CFD simulations conducted under different stress loadings during water volume injections. Figure 12 depicts the variations in the relative permeabilities of water (Kr_w) and oil (Kr_o) at the fracture–matrix interface for different water-saturation (S_w) and stress-loading conditions. It can be seen that as water saturation increases, the relative permeability of oil reduces nonlinearly. Water relative permeability has the opposite tendency of oil relative permeability, i.e., water relative permeability increases as water saturation increases. This is because injected water pushes the oil out of the fractured reservoir, reducing its relative permeability, while the water relative permeability increases.

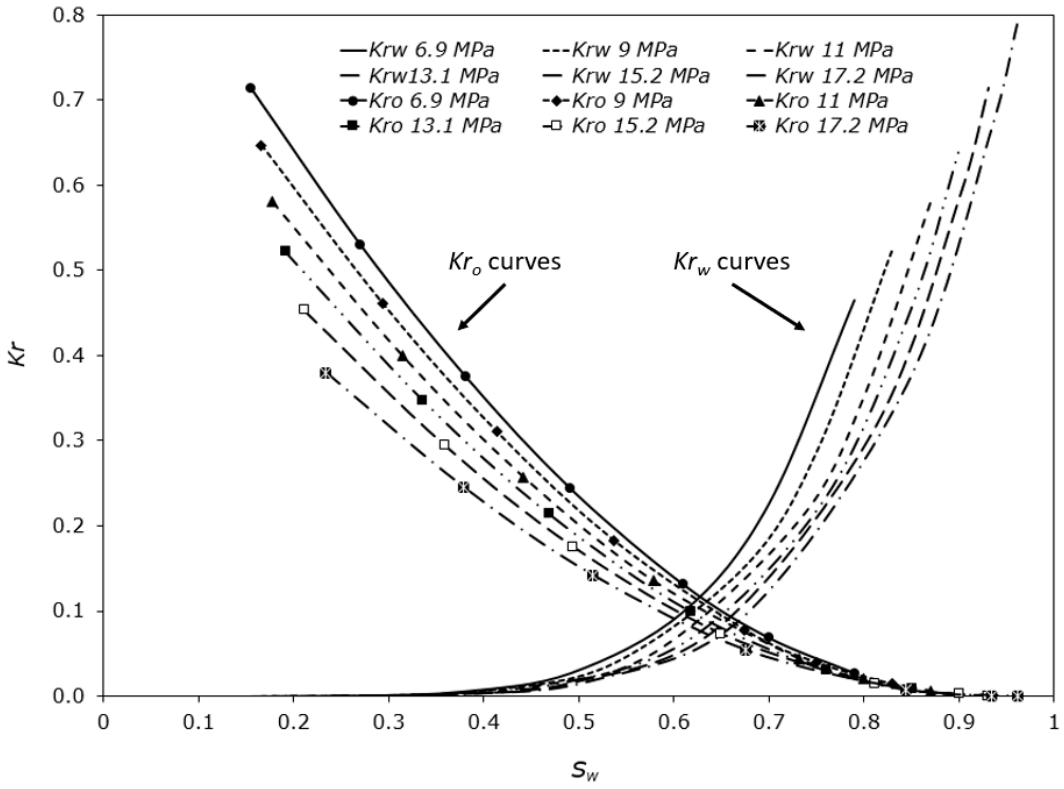

Figure 12. Relative permeability variations at different stress loadings.

6. Discussion

The estimated porosity from numerical modelling concurs with the relatively high Young's modulus and rock strength, indicating that Clashach's core sample is a moderately hard rock according to the US National Engineering Handbook [69]. The deformation of the core sample alters the pore volume (porosity) and the pore network. The decrease in the porosity of the reservoir under the action of externally applied stress enhances the oil recovery from the reservoir [70]. The study provides insights into the relationship between stress and porosity in naturally fractured tight reservoir samples. Understanding this relationship is crucial for predicting fluid flow behavior and devising strategies to enhance oil recovery from the reservoir. The Clashach core's permeability reduces by 1.3% with a nearly 0.13% reduction in porosity, which highlights the pore space's weak connectivity. The intact rock's contribution to the determined strain and conductivity of the fractured core decreases because of the minimal pore strain and low permeability. Moreover, this indicates that the intact rock's contribution to the determined strain and conductivity of the fractured core is low due to minimal pore strain and low permeability. This implies that the fractured rock's properties dominate the overall behavior of the rock mass rather than the intact rock. The results provide insights into the behavior of fracture apertures under externally applied stress and highlight the importance of understanding these phenomena in various geological and engineering applications.

In addition, when comparing the variations in k_f with the variations in k_{mat} (in Figure 6), it can be observed that the fracture permeability is much higher than the matrix permeability, as expected [7,71]. Furthermore, the decrease in fracture permeability is more significant than that in matrix permeability for the same stress loading. This is because fracture permeability is affected by rock compaction and fracture closure, but matrix permeability is affected by rock compaction. Thus, to upgrade computational efficiency, it is logical to obtain matrix and fracture permeabilities by coupling the fracture with the matrix, instead of modelling them separately. Consequently, based on the simulation results, the computational efficiency can be improved by coupling the disconnected and narrow aperture's effects under different external stress loadings. These findings show that stress-dependent fracture closure plays a significant role in the multiphase flow characteristics of fractures in subterranean formations. In terms of the external stress being applied to the rock matrix, it can be seen that it has a significant impact on the relative permeabilities of both oil and water, as well as on water saturation. It can be seen that when increasing external stress loading, the relative permeability of oil decreases, while the relative permeability of water increases. However, external stress also causes a shift in water saturation, which in turn affects the relative permeabilities. This is because the water saturation is dependent on the injected water volume V_w, as discussed earlier in Section 5.5. Thus, an in-depth understanding of the interdependencies between the injected water volume, water saturation and the relative permeabilities is essential for petroleum engineers when predicting oil recovery from fractured tight reservoirs, as this provides a quantifiable criterion for making informed decisions about the effectiveness of oil recovery methods.

7. Conclusions

Modelling transient multiphase fluid flow in naturally fractured tight reservoirs is a challenging task that requires careful consideration of the stress-dependent petrophysical properties and the stress-dependent flow characteristics, especially at the fracture–matrix interface. This study adopts a coupled FEM–CFD numerical modelling technique in order to accurately predict oil recovery from fractured reservoirs. The results obtained through the use of a well-validated coupled FEM–CFD model show that as external stress loading increases, the porosity and permeability of the naturally fractured tight reservoir decrease, which is expected under real-world conditions. Increasing the stress loading on the reservoir sample 1.5-fold, the matrix porosity decreases by 0.13% and the matrix permeability reduces by 1.3%. The intact rock's contribution to the determined strain and conductivity of the fractured core is low due to minimal pore strain and low permeability. It has been observed that the fracture aperture and its vertical displacement decrease as the external stress increases, reducing the mean fracture aperture. Therefore, stress also has a profound impact on fracture permeability, which was found to decrease by up to 29% as external loading increased from 6.9 MPa to 17.2 MPa. Moreover, the capillary pressure decreases due to an increase in stress loading at the fracture–matrix interface. The fracture–matrix interface becomes water-wet when the stress loading increases, while the relative permeability curves shift towards the right. These results provide meaningful insights into the multiphase flow behavior of naturally fractured tight reservoirs under externally applied stress and highlight the importance of understanding these phenomena in various geological and engineering applications. These findings are also invaluable for optimizing oil recovery strategies and making informed decisions in the field of petroleum engineering. Further research in this area can help refine models and improve the efficiency of oil recovery processes in fractured reservoirs. While the current study focuses on the effects of stress on multiphase flow at the fracture–matrix interface, further research could involve a more comprehensive analysis of dynamic stress changes, such as those induced by hydraulic fracturing or reservoir depletion. Incorporating real-time field data and extending the simulation to include thermal effects could provide deeper insights into the performance of enhanced oil recovery methods. Additionally, integrating machine-learning techniques to predict reservoir behavior under varying stress conditions could

significantly enhance the model's predictive capabilities and offer a more efficient approach to reservoir management.

Author Contributions: H.K.H. contributed to the conceptualization, data preparation, simulation, technical testing, writing, and interpretation. T.A., identified as the corresponding author, played a key role in the conceptualization, review, editing, feedback, supervision, project management, model accuracy assessments, and writing. All authors have read and agreed to the published version of the manuscript.

Funding: The research received no external funding.

Institutional Review Board Statement: Not applicable.

Informed Consent Statement: Not applicable.

Data Availability Statement: Data is contained within the article.

Conflicts of Interest: The authors declare no conflicts of interest.

References

1. Han, K.; Song, X.; Yang, H. The Pricing of Shale Gas: A Review. *J. Nat. Gas Sci. Eng.* **2021**, *89*, 103897. [CrossRef]
2. Suboyin, A.; Rahman, M.M.; Haroun, M. Hydraulic Fracturing Design Considerations and Optimal Usage of Water Resources for Middle Eastern Tight Gas Reservoirs. *ACS Omega* **2021**, *6*, 13433–13446. [CrossRef] [PubMed]
3. Shen, B.; Tao, Y.; Wang, G.; Fan, H.; Wang, X.; Sun, K. A New Method for Mobility Logging Evaluation Based on Flowing Porosity in Shale Oil Reservoirs. *Processes* **2023**, *11*, 1466. [CrossRef]
4. Li, Z.; Wu, W.; Hua, S.; Meng, X.; Zhou, N. Application of Foam Fluids in the Development of Unconventional Gas Reservoirs. *Front. Energy Res.* **2023**, *10*, 2018–2021. [CrossRef]
5. Hawez, H.K.; Sanaee, R.; Faisal, N.H. A Critical Review on Coupled Geomechanics and Fluid Flow in Naturally Fractured Reservoirs. *J. Nat. Gas Sci. Eng.* **2021**, *95*, 104150. [CrossRef]
6. Cui, G.; Cheng, W.; Xiong, W.; Chen, T.; Li, Y.; Feng, X.T.; Liu, J.; Elsworth, D.; Pan, Z. Influence of Well Types on Optimizing the Co-Production of Gas from Coal and Tight Formations. *Energy Fuels* **2022**, *36*, 6736–6754. [CrossRef]
7. Stanton-Yonge, A.; Mitchell, T.M.; Meredith, P.G. The Hydro-Mechanical Properties of Fracture Intersections: Pressure-Dependant Permeability and Effective Stress Law. *J. Geophys. Res. Solid Earth* **2023**, *128*, e2022JB025516. [CrossRef]
8. Hui, G.; Chen, Z.; Schultz, R.; Chen, S.; Song, Z.; Zhang, Z.; Song, Y.; Wang, H.; Wang, M.; Gu, F. Intricate Unconventional Fracture Networks Provide Fluid Diffusion Pathways to Reactivate Pre-Existing Faults in Unconventional Reservoirs. *Energy* **2023**, *282*, 128803. [CrossRef]
9. Kollár, L.E.; Mishra, R.; Asim, T. Particle Size Effects on Optimal Sizing and Lifetime of Pipelines Transporting Multi-Sized Solid-Liquid Mixtures. *Procedia CIRP* **2013**, *11*, 317–322. [CrossRef]
10. Viswanathan, H.S.; Ajo-Franklin, J.; Birkholzer, J.T.; Carey, J.W.; Guglielmi, Y.; Hyman, J.D.; Karra, S.; Pyrak-Nolte, L.J.; Rajaram, H.; Srinivasan, G.; et al. From Fluid Flow to Coupled Processes in Fractured Rock: Recent Advances and New Frontiers. *Rev. Geophys.* **2022**, *60*, e2021RG000744. [CrossRef]
11. Abdideh, M.; Dastyaft, F. Stress Field Analysis and Its Effect on Selection of Optimal Well Trajectory in Directional Drilling (Case Study: Southwest of Iran). *J. Pet. Explor. Prod. Technol.* **2022**, *12*, 835–849. [CrossRef]
12. Hawez, H.K.; Asim, T. Impact of Regional Pressure Dissipation on Carbon Capture and Storage Projects: A Comprehensive Review. *Energies* **2024**, *17*, 1889. [CrossRef]
13. Li, Z.; Hu, X. Determining Triaxial Stress Sensitivity of Oil Reservoir Rocks without Fluid Flooding. *Geofluids* **2021**, *2021*, 6668799. [CrossRef]
14. Schimmel, M.T.W.; Hangx, S.J.T.; Spiers, C.J. Impact of Chemical Environment on Compaction Creep of Quartz Sand and Possible Geomechanical Applications. *J. Geophys. Res. Solid Earth* **2019**, *124*, 5584–5606. [CrossRef]
15. Subbiah, S.K.; Samsuri, A.; Mohamad-Hussein, A.; Jaafar, M.Z.; Chen, Y.R.; Kumar, R.R. Root Cause of Sand Production and Methodologies for Prediction. *Petroleum* **2021**, *7*, 263–271. [CrossRef]
16. Agheshlui, H.; Sedaghat, M.H.; Matthai, S. Stress Influence on Fracture Aperture and Permeability of Fragmented Rocks. *J. Geophys. Res. Solid Earth* **2018**, *123*, 3578–3592. [CrossRef]
17. Cao, N.; Lei, G.; Dong, P.; Li, H.; Wu, Z.; Li, Y. Stress-Dependent Permeability of Fractures in Tight Reservoirs. *Energies* **2019**, *12*, 117. [CrossRef]
18. Feng, Y.; Tang, H.; Tang, H.; Leng, Y.; Shi, X.; Liu, J.; Wang, Z.; Deng, C. Influence of Geomechanics Parameters on Stress Sensitivity in Fractured Reservoir. *Front. Earth Sci.* **2023**, *11*, 1134260. [CrossRef]
19. Haghi, A.H.; Chalaturnyk, R. Experimental Characterization of Hydrodynamic Properties of a Deformable Rock Fracture. *Energies* **2022**, *15*, 6769. [CrossRef]
20. Shen, W.; Ma, T.; Li, X.; Sun, B.; Hu, Y.; Xu, J. Fully Coupled Modeling of Two-Phase Fluid Flow and Geomechanics in Ultra-Deep Natural Gas Reservoirs. *Phys. Fluids* **2022**, *34*, 043101. [CrossRef]

21. Yang, Z.D.; Wang, Y.; Zhang, X.Y.; Qin, M.; Su, S.W.; Yao, Z.H.; Liu, L. Numerical Simulation of a Horizontal Well With Multi-Stage Oval Hydraulic Fractures in Tight Oil Reservoir Based on an Embedded Discrete Fracture Model. *Front. Energy Res.* **2020**, *8*, 601107. [CrossRef]
22. Tan, Q.; Kang, Y.; You, L.; Xu, C.; Zhang, X.; Xie, Z. Stress-Sensitivity Mechanisms and Its Controlling Factors of Saline-Lacustrine Fractured Tight Carbonate Reservoir. *J. Nat. Gas Sci. Eng.* **2021**, *88*, 103864. [CrossRef]
23. Haghi, A.H.; Chalaturnyk, R.; Geiger, S. New Semi-Analytical Insights Into Stress-Dependent Spontaneous Imbibition and Oil Recovery in Naturally Fractured Carbonate Reservoirs. *Water Resour. Res.* **2018**, *54*, 9605–9622. [CrossRef]
24. Peretomode, E.; Oluyemi, G.; Faisal, N.H. Oilfield Chemical-Formation Interaction and the Effects on Petrophysical Properties: A Review. *Arab. J. Geosci.* **2022**, *15*, 1223. [CrossRef]
25. Al-Kindi, I.; Babadagli, T. Phase Behavior of Single and Multi-Component Liquid Hydrocarbons in Real Reservoir Rocks. *Sci. Rep.* **2023**, *13*, 4507. [CrossRef]
26. Ghanizadeh, A.; Song, C.; Clarkson, C.R.; Younis, A. Relative Permeability of Tight Hydrocarbon Systems: An Experimental Study. *Fuel* **2021**, *294*, 119487. [CrossRef]
27. Xu, S.; Guo, J.; Feng, Q.; Ren, G.; Li, Y.; Wang, S. Optimization of Hydraulic Fracturing Treatment Parameters to Maximize Economic Benefit in Tight Oil. *Fuel* **2022**, *329*, 125329. [CrossRef]
28. Hawez, H.; Sanaee, R.; Faisal, N.H. Multiphase Flow Modelling in Fractured Reservoirs Using a Novel Computational Fluid Dynamics Approach. In Proceedings of the 55th U.S. Rock Mechanics/Geomechanics Symposium, Virtual, 18–25 June 2021.
29. Li, S.; Zhao, H.; Cheng, T.; Wang, J.; Gai, J.; Zou, L.; He, T. The Analysis of Hydraulic Fracture Morphology and Connectivity under the Effect of Well Interference and Natural Fracture in Shale Reservoirs. *Processes* **2023**, *11*, 2627. [CrossRef]
30. Ran, Q.; Zhou, X.; Dong, J.; Xu, M.; Ren, D.; Li, R. Study on the Fracture Propagation in Multi-Horizontal Well Hydraulic Fracturing. *Processes* **2023**, *11*, 1995. [CrossRef]
31. Asim, T. *Capacity Testing of X-Stream Valves for Single-Component Single-Phase Flows*; Weir Valves and Controls: Elland, UK, 2013.
32. Gao, C. *A Coupled Geomechanics and Reservoir Simulator and Its Application to Reservoir Development*; The University of Texas at Austin: Austin, TX, USA, 2019.
33. Sangnimnuan, A.; Li, J.; Wu, K. Development of Coupled Two-Phase Flow and Geomechanics Model to Predict Stress Evolution in Unconventional Reservoirs with Complex Fracture Geometry. *J. Pet. Sci. Eng.* **2021**, *196*, 108072. [CrossRef]
34. Ashworth, M.; Doster, F. An Open Source Numerical Framework for Dual-Continuum Geomechanical Simulation. In Proceedings of the Society of Petroleum Engineers—SPE Reservoir Simulation Conference 2019, RSC 2019, Galveston, TX, USA, 10–11 April 2019; Society of Petroleum Engineers: Aberdeen, UK, 2019.
35. Berger, L.; Bordas, R.; Kay, D.; Tavener, S. A Stabilized Finite Element Method for Finite-Strain Three-Field Poroelasticity. *Comput. Mech.* **2017**, *60*, 51–68. [CrossRef]
36. Sanaee, R.; Oluyemi, G.F.; Hossain, M.; Oyeneyin, M.B. Stress Effects on Flow Partitioning in Fractured Reservoirs: Equivalent Porous Media versus Poro-Elasticity Coupled Modeling. In Proceedings of the 47th U.S. Rock Mechanics/Geomechanics Symposium, San Francisco, CA, USA, 23–26 June 2013; American Rock Mechanics Association: Alexandria, VA, USA, 2013; Volume 3, pp. 2329–2337.
37. Cai, L. *Matrix-Fracture Interaction Analysis in Fractured Unconventional Gas Reservoir*; Colorado School of Mines: Golden, CO, USA, 2014.
38. Jiang, J.; Yang, J. Coupled Fluid Flow and Geomechanics Modeling of Stress-Sensitive Production Behavior in Fractured Shale Gas Reservoirs. *Int. J. Rock Mech. Min. Sci.* **2018**, *101*, 1–12. [CrossRef]
39. Liu, X.; Zhu, G.; Asim, T.; Mishra, R. Combustion Characterization of Hybrid Methane-Hydrogen Gas in Domestic Swirl Stoves. *Fuel* **2023**, *333*, 126413. [CrossRef]
40. Charlton, M.; Mishra, R.; Asim, T. The Effect of Manufacturing Method-Induced Roughness on Severe Service Control Valve Performance. In Proceedings of the 6th International and 43rd National Conference on Fluid Mechanics and Fluid Power, Allahabad, India, 15–17 December 2016.
41. Jackson, G.W.; James, D.F. The Permeability of Fibrous Porous Media. *Can. J. Chem. Eng.* **1986**, *64*, 364–374. [CrossRef]
42. Mavko, G.; Mukerji, T.; Dvorkin, J. Elasticity and Hooke's Law. In *The Rock Physics Handbook*; Cambridge University Press: Cambridge, UK, 2020; pp. 37–120.
43. Zhao, Y.; Liu, H.H. An Elastic Stress-Strain Relationship for Porous Rock under Anisotropic Stress Conditions. *Rock Mech. Rock Eng.* **2012**, *45*, 389–399. [CrossRef]
44. Liu, H.H.; Rutqvist, J.; Berryman, J.G. On the Relationship between Stress and Elastic Strain for Porous and Fractured Rock. *Int. J. Rock Mech. Min. Sci.* **2009**, *46*, 289–296. [CrossRef]
45. Cai, Y.; Sun, H. Basic Equations and Governing Equations. In *Solutions for Biot's Poroelastic Theory in Key Engineering Fields*; Elsevier Ltd.: Amsterdam, The Netherlands, 2017; pp. 1–8. ISBN 9780128126493.
46. Tachibana, S.; Ito, S.; Iizuka, A. Constitutive Model with a Concept of Plastic Rebound for Expansive Soils. *Soils Found.* **2020**, *60*, 179–197. [CrossRef]
47. Dazel, O.; Dauchez, N. The Finite Element Method for Porous Materials. In *Materials and Acoustics Handbook*; Bruneau, M., Potel, C., Eds.; John Wiley & Sons: Hoboken, NJ, USA, 2009; pp. 327–338. ISBN 9781848210745.
48. Alymann, J.B. Poroelastic Effects in Reservoir Modelling. Ph.D. Thesis, Universität Karlsruhe, Karlsruhe, Germany, 2010.

49. Lewis, R.W.; Schrefler, B.A. *The Finite Element Method in the Static and Dynamic Deformation and Consolidation of Porous*, 2nd ed.; Wiley: Hoboken, NJ, USA, 1999.
50. Simo, J.C.; Taylor, R.L.; Pister, K.S. Variational and Projection Methods for the Volume Constraint in Finite Deformation Elasto-Plasticity. *Comput. Methods Appl. Mech. Eng.* **1985**, *51*, 177–208. [CrossRef]
51. Federico, S.; Grillo, A. Elasticity and Permeability of Porous Fibre-Reinforced Materials under Large Deformations. *Mech. Mater.* **2012**, *44*, 58–71. [CrossRef]
52. *Abaqus 6.11/Theory Manual*; Simulia Corp.: Providence, RI, USA, 2011.
53. Saxena, V.; Krief, M.; Adam, L. *Handbook of Borehole Acoustics and Rock Physics for Reservoir Characterization*; Elsevier: Amsterdam, The Netherlands, 2018; ISBN 9780128122044.
54. Lay, T.; Wallace, T.C. Elasticity and Seismic Waves. In *Modern Global Seismology*; Academic Press: Cambridge, MA, USA, 1995; Volume 58, pp. 34–69. ISBN 9780127328706.
55. Stalker, R.; Graham, G.M.; Oluyemi, G. Modelling Staged Diversion Treatments and Chemical Placement in the Presence of Near-Wellbore Fractures. *Proc.-SPE Int. Symp. Oilf. Chem.* **2009**, *2*, 745–757. [CrossRef]
56. Stalker, R.; Graham, G.M.; Oliphant, D.; Smillie, M. Potential Application of Viscosified Treatments for Improved Bullhead Scale Inhibitor Placement in Long Horizontal Wells—A Theoretical and Laboratory Examination. In Proceedings of the SPE Sixth International Symposium on Oilfield Scale, Exploring the Boundaries of Scale Control. Aberdeen, UK, 26–27 May 2004; pp. 137–150. [CrossRef]
57. Singh, D.; Charlton, M.; Asim, T.; Mishra, R.; Townsend, A.; Blunt, L. Quantification of Additive Manufacturing Induced Variations in the Global and Local Performance Characteristics of a Complex Multi-Stage Control Valve Trim. *J. Pet. Sci. Eng.* **2020**, *190*, 107053. [CrossRef]
58. Taimoor, A. Computational Fluid Dynamics Based Diagnostics and Optimal Design of Hydraulic Capsule Pipelines. Ph.D. Thesis, University of Huddersfield, Huddersfield, UK, 2013.
59. Ma, J.; Wang, J. A Stress-Induced Permeability Evolution Model for Fissured Porous Media. *Rock Mech. Rock Eng.* **2016**, *49*, 477–485. [CrossRef]
60. Ren, X.; Zhao, Y.; Deng, Q.; Kang, J.; Li, D.; Wang, D. A Relation of Hydraulic Conductivity—Void Ratio for Soils Based on Kozeny-Carman Equation. *Eng. Geol.* **2016**, *213*, 89–97. [CrossRef]
61. Liu, X.; Asim, T.; Zhu, G.; Mishra, R. Theoretical and Experimental Investigations on the Combustion Characteristics of Three Components Mixed Municipal Solid Waste. *Fuel* **2020**, *267*, 117183. [CrossRef]
62. Bai, M.; Elsworth, D. Modeling of Subsidence and Stress-Dependent Hydraulic Conductivity for Intact and Fractured Porous Media. *Rock Mech. Rock Eng.* **1994**, *27*, 209–234. [CrossRef]
63. Asim, T.; Mishra, R.; Ubbi, K.; Zala, K. Computational Fluid Dynamics Based Optimal Design of Vertical Axis Marine Current Turbines. *Procedia CIRP* **2013**, *11*, 323–327. [CrossRef]
64. Bogdanov, I.I.; Mourzenko, V.V.; Thovert, J.F.; Adler, P.M. Effective Permeability of Fractured Porous Media in Steady State Flow. *Water Resour. Res.* **2003**, *39*, 1023. [CrossRef]
65. Zhang, J.; Standifird, W.B.; Roegiers, J.C.; Zhang, Y. Stress-Dependent Fluid Flow and Permeability in Fractured Media: From Lab Experiments to Engineering Applications. *Rock Mech. Rock Eng.* **2007**, *40*, 3–21. [CrossRef]
66. Brooks, R.H.; Corey, A.T. Properties of Porous Media Affecting Fluid Flow. *J. Irrig. Drain. Div.* **1966**, *92*, 61–88. [CrossRef]
67. Miao, J.; Zhong, C. Dynamic Variation of Water Saturation and Its Effect on Aqueous Phase Trapping Damage during Tight Sandstone Gas Well Production. *ACS Omega* **2021**, *6*, 5166–5175. [CrossRef]
68. Zaeri, M.R.; Shahverdi, H.; Hashemi, R.; Mohammadi, M. Impact of Water Saturation and Cation Concentrations on Wettability Alteration and Oil Recovery of Carbonate Rocks Using Low-Salinity Water. *J. Pet. Explor. Prod. Technol.* **2019**, *9*, 1185–1196. [CrossRef]
69. NRCS. Chapter 4-Engineering Classification of Rock Materials. In *Part 631-Geology*; 631.0401 Rock Material Properties, Section (c); NRCS: Washington, DC, USA, 2012.
70. Lima, R.O.; do Nascimento Guimarães, L.J.; Pereira, L.C. Evaluating Geomechanical Effects Related to the Production of a Brazilian Reservoir. *J. Pet. Explor. Prod.* **2021**, *11*, 2661–2678. [CrossRef]
71. Cheng, C.; Herrmann, J.; Wagner, B.; Leiss, B.; Stammeier, J.A.; Rybacki, E.; Milsch, H. Long-Term Evolution of Fracture Permeability in Slate: An Experimental Study with Implications for Enhanced Geothermal Systems (EGS). *Geosciences* **2021**, *11*, 443. [CrossRef]